

Three-Window Transformation Cross-Talk Correction for Simultaneous Dual-Isotope Imaging

Karin Knešaurek and Josef Machac

Division of Nuclear Medicine, Mount Sinai Medical Center, New York, New York

We developed and tested a new transformation cross-talk correction method for simultaneous dual-isotope SPECT imaging, which uses information from three energy windows in a simultaneous $^{18}\text{F}/^{99\text{m}}\text{Tc}$ cardiac phantom study. **Methods:** The method combines the previously reported "three-window" technique and transformation cross-talk correction methods. In the three-window technique, the images from the third energy "scatter" window are usually multiplied by a constant factor to obtain the estimates of the cross-talk. However, such an approach neglects differences in the spatial distribution between cross-talk photons in different energy windows. The transformation method is based on the assumption that the transformations, which convert the images from one energy window into the other energy windows, are known. These transformations were found by measuring the point-spread functions in different energy windows for both isotopes in water. The transformation method takes into account the different spatial distributions of the primary and scatter cross-talk photons in the different energy windows. Here, we are assuming that the imaging system and the image transformations between different energy windows are shift-invariant and linear. Thus, the new method is described by two convolution equations applied in frequency space. In addition to the cross-talk correction, the restoration filters were also applied to the resulting corrected images. The new method was performed on the simultaneous $^{18}\text{F}/^{99\text{m}}\text{Tc}$ cardiac phantom study. Three separate studies were acquired in our phantom study: two single-isotope studies and one dual-isotope study. The single-isotope images were used as references. The contrast between the left ventricle cavity and the myocardium was used in transaxial slices as a parameter to evaluate results of the dual-isotope correction method with restoration. **Results:** The contrast improvement in the dual-isotope corrected images in both energy windows, i.e., the $^{99\text{m}}\text{Tc}$ primary window (140 keV) and the ^{18}F primary window (511 keV), was significant. The corrected 511-keV, dual-isotope image had a contrast of 0.74 compared to 0.60, which was the value in the noncorrected dual-isotope image. The improvement of the contrast in the corrected, dual-isotope 511-keV image was exclusively a result of the restoration correction. The restoration-corrected, 511-keV, single-isotope ^{18}F image had the same contrast (0.74). For the dual-isotope, 140-keV transaxial slice, first, the contrast improved from 0.78 to 0.85 after cross-talk correction, and, then, it finally reached 0.92 after additional restoration correction. The contrast in the 140-keV, single-isotope $^{99\text{m}}\text{Tc}$ image after restoration correction improved from 0.87 to 0.95. **Conclusion:** The three-window transformation dual-isotope correction method with restoration significantly improves the contrast between the left ventricle cavity and the myocardium of the simultaneous $^{18}\text{F}/^{99\text{m}}\text{Tc}$ SPECT imaging.

Key Words: simultaneous dual-isotope imaging; cross-talk correction; SPECT

J Nucl Med 1997; 38:1992–1998

The advantages of simultaneous dual-isotope imaging over conventional single-isotope or sequential dual-isotope imaging lie in the shorter duration of procedures, with an identical geometrical registration of the different isotope images. The

reduction in patient study time decreases the risk of artifacts due to patient motion and improves patient throughput and comfort. The geometrically identical registration of the different isotope images facilitates image interpretation and quantification. However, quantitative and qualitative simultaneous dual-isotope imaging is limited by the contribution of cross-talk. Cross-talk is the movement of scattered and primary photons from one radionuclide into the other radionuclide's primary photopeak energy window (1,2).

Simultaneous dual-isotope imaging has been used in brain scintigraphy to assess cerebral perfusion and recurrence of brain tumor (3). It has also been used in hyperparathyroidism (4) and in the evaluation of lung function (5). Dual-isotope procedures have numerous applications in various types of myocardial imaging: localization of cardiac infarct (6), determination of prognosis after acute myocardial infarction (7,8), assessment of inflammatory myocardial disease (9) and quantitative estimation of infarct size (10). The hybrid ^{201}Tl – $^{99\text{m}}\text{Tc}$ -sestamibi rest-stress imaging was used for the diagnosis of coronary artery disease (11,12), and dual-isotope [^{18}F]FDG/ ^{201}Tl and [^{18}F]FDG/ $^{99\text{m}}\text{Tc}$ -sestamibi (13–15) have been used for determination of myocardial viability.

Yang et al. (16) and Hademenos et al. (17) reported previously on simultaneous dual-isotope techniques that make use of a third energy window to estimate the cross-talk. These methods were mostly based on "correction factors" rather than on transformations that would take into account differences in spatial distribution between primary and scatter images. Moore et al. (18) reported a simulation $^{99\text{m}}\text{Tc}/^{201}\text{Tl}$ study in which they estimated $^{99\text{m}}\text{Tc}$ down-scatter into the ^{201}Tl primary 70-keV window by blurring the $^{99\text{m}}\text{Tc}$ photopeak and third scattered-window image by different Gaussian filters. These methods were prereconstruction corrections performed on the projections. A postreconstruction cross-talk correction method, based on convolution technique, has been developed at our center using a cardiac phantom (1). This new method takes an innovative approach for cross-talk correction by accounting for the differences in the spatial distribution of the primary and scatter photons.

Here, we present a new transformation cross-talk correction method for simultaneous dual-isotope SPECT imaging that uses information from three energy windows. The method was tested in a simultaneous $^{18}\text{F}/^{99\text{m}}\text{Tc}$ cardiac phantom study. However, it can be applied to other dual-isotope studies, e.g., a $^{201}\text{Tl}/^{99\text{m}}\text{Tc}$ study. In addition to cross-talk correction, restoration filters (19–23) were applied to compensate for the effects of system blurring, scatter radiation, septal penetration and noise.

MATERIALS AND METHODS

Imaging Protocol

To calibrate the system, the single-isotope $^{99\text{m}}\text{Tc}$ and ^{18}F point-source images were acquired in a water-filled cylindrical phantom with a diameter of 23 cm. The point source was placed at distances of 0 cm, 2.5 cm, 5 cm, 7.5 cm and 9 cm from the center

Received Oct. 15, 1996; revision accepted Feb. 26, 1997.

For correspondence or reprints contact: Karin Knešaurek, PhD, Division of Nuclear Medicine, Box 1141, One Gustave L. Levy Place, New York, NY 10029.

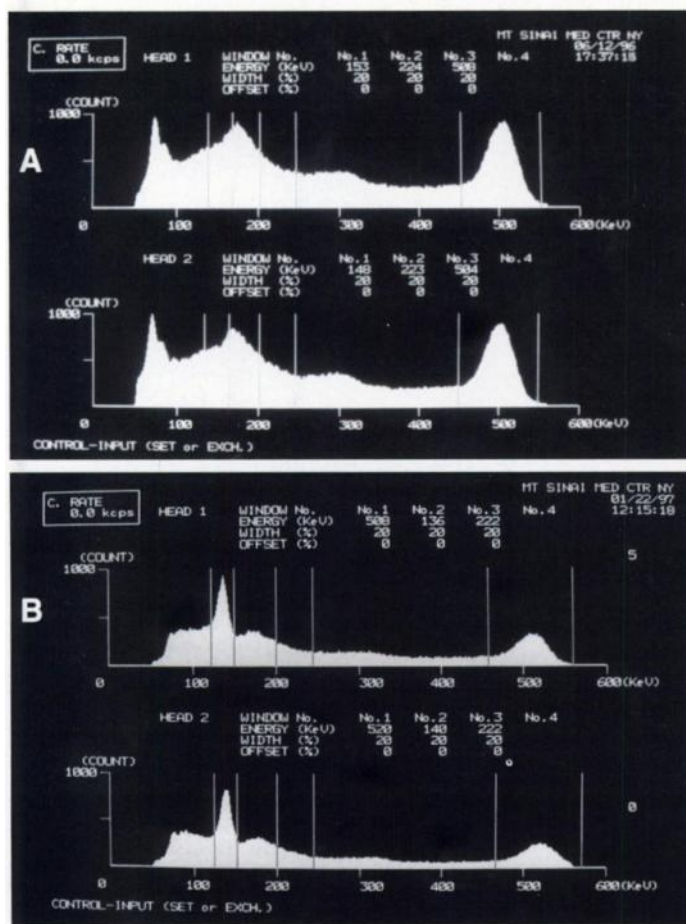


FIGURE 1. Energy spectrum on our system with an UHE, 511-keV collimator of ^{18}F (A) and the same activity of ^{18}F and $^{99\text{m}}\text{Tc}$ (B). The three 20% energy windows used are also shown. The back-scatter, at 170 keV, is prominent.

of the phantom. The FWHM was measured for all point sources in the radial and tangential directions. All acquisitions were performed with three 20% wide energy windows each. The first energy window was centered at 511-keV, the second was at 250 keV and third was at 140 keV (Fig. 1). The reconstructed point spread functions (PSFs), at a distance of 5 cm from the center of the cylinder (Fig. 2), were used to create transformation functions and restoration filters. The choice of this PSF was made to correspond to the average position of the heart within the phantom. SPECT acquisitions were performed in step-and-shoot mode with a 64×64 acquisition frame matrix size and a zoom of 1.5. The time per frame was 40 sec. The 64 frames were acquired over 360° . The pixel size in the acquisition and reconstructed images was 6.08 mm. SPECT data were processed using standard reconstruction software based on a filter back-projection method. A Butterworth filter of fifth order and a cutoff frequency of 0.23 were applied in the reconstruction for all studies. No attenuation or scatter correction was performed. A dual-headed SPECT system (T22 gamma camera; SMV, Twinsburg, Ohio) with an ultra-high-energy (UHE) collimator was used for all dual-window acquisitions. The UHE parallel-hole collimator for 511-keV imaging had the following specifications: diameter of the hexagonal holes, 3.4 mm; hole length, 65.0 mm; and septal thickness, 3.0 mm. The collimator cores were mounted in an all-lead frame designed for 511-keV imaging. Planar resolutions as a function of distance for the UHE collimator, measured in air with a $^{99\text{m}}\text{Tc}$ point source, were FWHM = 3.9 mm, 10.6 mm and 14.0 mm for distances of 0 cm, 10 cm and 15 cm, respectively. The same planar resolutions measured with a ^{18}F point source gave FWHM = 5.3 mm, 13.9 mm and 18.2 mm for distances of 0 cm, 10 cm and 15 cm, respectively.

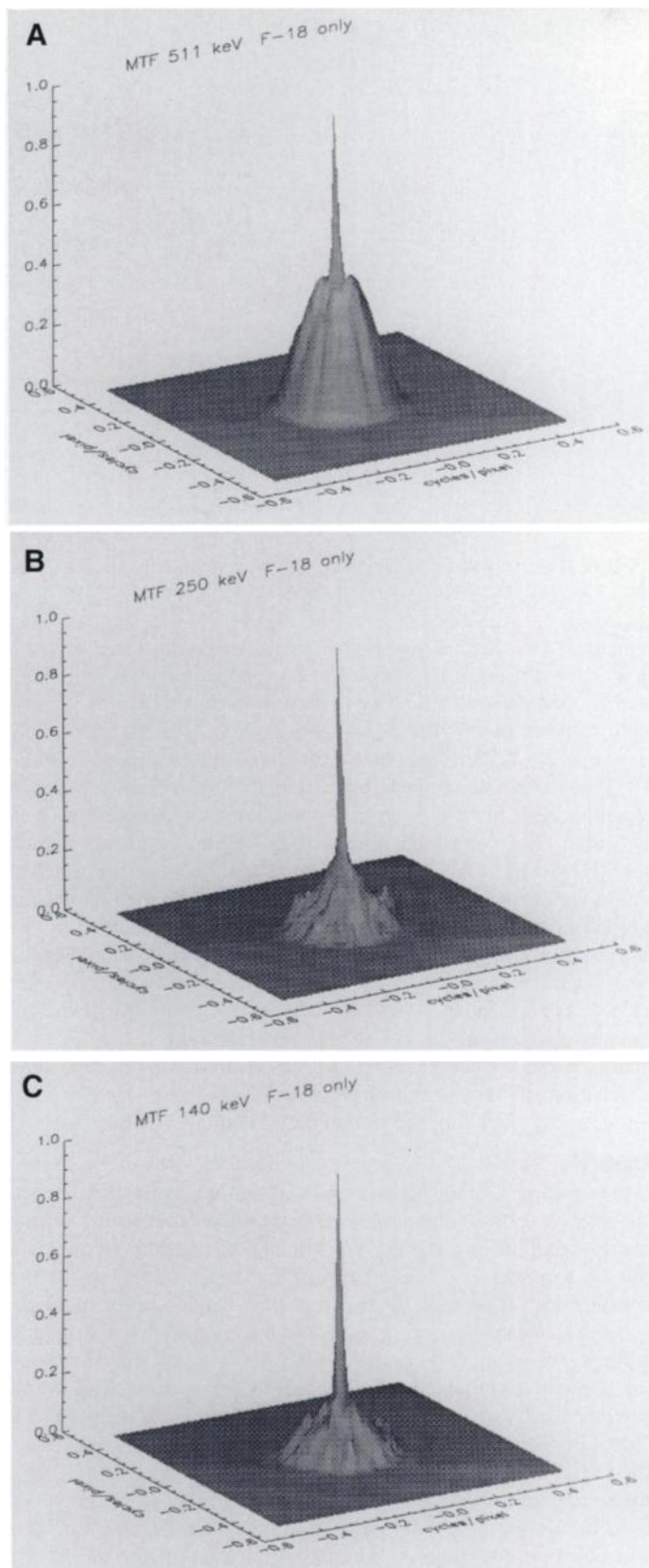


FIGURE 2. Reconstructed and normalized MTFs obtained from acquisition of a ^{18}F point source at a distance of 5 cm from the center of the water-filled cylinder at the 511-keV window (A), at the 250-keV window (B) and at the 140-keV window (C).

The s.d. was less than 0.5 mm in all measurements and was obtained from three measurements. The energy resolution of the system at 140 keV was 9.8% (Fig. 1).

A nonuniform RH-2 thorax-heart phantom (Kyoto Scientific

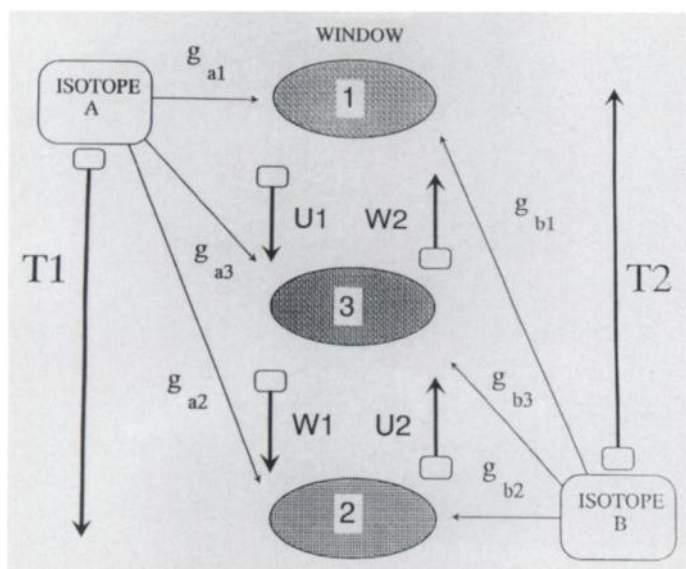


FIGURE 3. Schematic presentation of the notation used for simultaneous, dual-isotope, three-window transformation cross-talk correction technique.

Specimen Co., Ltd., Kyoto, Japan) was imaged in three separate SPECT acquisitions: two single-isotope acquisitions and one dual-isotope acquisition. The first phantom acquisition was single-isotope, performed with ^{18}F , using an activity of 24.05 MBq in the left ventricle wall. Immediately after the first acquisition, 24.05 MBq of $^{99\text{m}}\text{Tc}$ was injected into the left ventricle wall, and a second acquisition was performed with both isotopes present. Two days after the second acquisition, a third, single-isotope acquisition with 24.05 MBq of $^{99\text{m}}\text{Tc}$ in the left ventricle was performed. The single-isotope images were used as references. The total number of counts in the projection images varied with the angle. In the dual-isotope study, the total numbers of counts were between 20,100 and 10,250 in the 511-keV window and between 32,050 and 18,450 counts in the 140-keV window. Counts were mostly concentrated in the 20×20 pixel area showing the projection image of the cardiac phantom. In the phantom studies, the same acquisition and reconstruction parameters were used as in the point source study including the same energy window setting.

Theory

One way to correct for cross-talk in simultaneous dual-isotope imaging is to find transformations that convert the images of one energy window into the scattered images as seen through other energy windows (I). These transformations are analogs of the precalibrated cross-talk fractions in dual-isotope well counting. They depend on the system used, the energy window setting and the isotopes applied. They can be found by using single-isotope studies with simultaneous dual-energy window acquisitions. The other approach to correct for cross-talk is to use images from a third ($16,17$) and even a fourth energy window (13) to estimate cross-talk in the window of interest. The images from these additional windows, appropriately scaled, give an estimate of cross-talk in terms of total number of counts and spatial distribution of cross-talk photons. Here, a combination of the previously published transformation method and "three-window" correction is presented. The three-window transformation method can be described as follows.

The notation used is presented in Figure 3. The subscripts "a" and "b" refer to isotope a (^{18}F) and isotope b ($^{99\text{m}}\text{Tc}$), respectively. The photopeak energy window of isotope a is denoted "1," and the photopeak energy window of isotope b is denoted "2." The third window is denoted "3." In this notation, for example, the subscript "a2" refers to the isotope a as seen in the energy window 2. The

images recorded in a three-energy window collection are g_1 , g_2 and g_3 . The following equations then result:

$$g_1 = g_{a1} + g_{b1}, \quad \text{Eq. 1}$$

$$g_2 = g_{a2} + g_{b2}, \quad \text{Eq. 2}$$

$$g_3 = g_{a3} + g_{b3}. \quad \text{Eq. 3}$$

Now we can assume that it is possible to find a transformation between different energy windows, as shown in Figure 3. This is described by:

$$g_{a2} = T_1\{g_{a1}\}, \quad \text{Eq. 4}$$

$$g_{b1} = T_2\{g_{b2}\}, \quad \text{Eq. 5}$$

$$g_{a2} = W_1\{g_{a3}\}, \quad \text{Eq. 6}$$

$$g_{b1} = W_2\{g_{b3}\}, \quad \text{Eq. 7}$$

$$g_{a3} = U_1\{g_{a1}\}, \quad \text{Eq. 8}$$

$$g_{b3} = U_2\{g_{b2}\}, \quad \text{Eq. 9}$$

where T_1 , T_2 , W_1 , W_2 , U_1 and U_2 are transformation functions, defined as the functions which, when convolved with one energy window image, give a scattered image as viewed at other energy windows. Solving Equations 1, 2, 4 and 5 gives:

$$g_{a1} = (I - T_2 \circ T_1)^{-1}\{g_1 - T_2\{g_2\}\} \quad \text{Eq. 10}$$

and

$$g_{b2} = (I - T_1 \circ T_2)^{-1}\{g_2 - T_1\{g_1\}\}, \quad \text{Eq. 11}$$

where \circ denotes the composition of two transformations and I denotes identity transformation, i.e., $I\{g_{ij}\} = g_{ij}$. This identity is a result of our previously published dual-isotope transformation cross-talk correction method (I). Using the information from the third window, i.e., Equations 1–9, in the same way, one can obtain (see Appendix):

$$g_{a1} = (I - W_2 \circ U_1)^{-1}\{g_1 - W_2\{g_3\}\} \quad \text{Eq. 12}$$

and

$$g_{b2} = (I - W_1 \circ U_2)^{-1}\{g_2 - W_1\{g_3\}\}. \quad \text{Eq. 13}$$

The difference between Equations 10 and 11 and Equations 12 and 13 is that the latter equations are using a dual-isotope image from the third window, g_3 , in addition to g_1 and g_2 .

Transformations T_1 , T_2 , W_1 , W_2 , U_1 and U_2 can be general, nonstationary transformations. However, we assumed that they are linear and shift-invariant and that they can be represented by convolution. For example, $g_{a2} = T_1\{g_{a1}\} = g_{a1} * t_1$, where $*$ denotes convolution. In this notation, the kernel is denoted with the same lowercase letter (in the real domain) as in the operator itself and with the same uppercase letter in the Fourier domain. Equations 10–13 are much simpler and are given in Fourier space as:

$$G_{a1} = (G_1 - G_2 \times T_2)/(I - T_1 \times T_2), \quad \text{Eq. 14}$$

$$G_{b2} = (G_2 - G_1 \times T_1)/(I - T_1 \times T_2), \quad \text{Eq. 15}$$

and

$$G_{a1} = (G_1 - G_3 \times W_2)/(I - W_2 \times U_1), \quad \text{Eq. 16}$$

$$G_{b2} = (G_2 - G_3 \times W_1)/(I - W_1 \times U_2), \quad \text{Eq. 17}$$

where uppercase characters refer to the frequency space representation of the real space functions, and \times denotes multiplication.

The transformation functions, T_1 , T_2 , W_1 , W_2 , U_1 and U_2 , are defined as the functions that, when convolved with one energy window image, give a scattered image as viewed at other energy windows. They are given as the ratio of the modulation transfer function (MTF), i.e., $T_1 = \text{MTF}_{a2}/\text{MTF}_{a1}$; $T_2 = \text{MTF}_{b1}/\text{MTF}_{b2}$; $W_1 = \text{MTF}_{a2}/\text{MTF}_{a3}$; $W_2 = \text{MTF}_{b1}/\text{MTF}_{b3}$; $U_1 = \text{MTF}_{a3}/\text{MTF}_{a1}$; and $U_2 = \text{MTF}_{b3}/\text{MTF}_{b2}$.

Equations 14 and 15 represent the dual-isotope convolution cross-talk correction method when only two energy windows are used. However, Equations 16 and 17 represent the dual-isotope, three-window convolution cross-talk correction method.

Having all these MTFs from point-source measurements, we can apply restoration correction in addition to the cross-talk correction. In this case, instead of finding single-isotope photopeak images, g_{a1} and g_{b2} , the goal is to obtain the estimates of the true isotope distributions, f_a and f_b . From Figure 3 it follows that:

$$F_a = G_{a1}/\text{MTF}_{a1} \quad \text{Eq. 18}$$

and

$$F_b = G_{b2}/\text{MTF}_{b2}, \quad \text{Eq. 19}$$

where F_a and F_b represent Fourier transforms of the isotope distributions f_a and f_b , respectively.

Practical Creation of the Transformation Functions and Restoration Filters

The transformation functions, T_1 , T_2 , W_1 , W_2 , U_1 and U_2 , as well as the estimates of the isotope distributions f_a and f_b , are given by the deconvolution relations described above. However, the deconvolution process is ill-conditioned. This ill-conditioning is emphasized even more by the neglect of attenuation effects and noise. There are several ways to constrain the deconvolution process (19–24). The MTFs used for creation of the transformation functions and restoration filters (Fig. 2) correspond to the point sources placed at a distance of 5 cm from the center of a uniformly filled cylinder. In the calculation of the transformation functions and restored images, an additional term, $\gamma = 10^{-6}$, was added in the denominator. This term served as a regularization function, which allowed the solution of a potentially ill-posed problem.

First, the three-window transformation cross-talk correction was applied, based on Equations 16 and 17, and then followed by a restoration correction (Equations 18 and 19). The Butterworth low-pass filter (LPF) of order $n = 7$ and cutoff frequency of $f = 0.172$ cycles/pixel were applied to create transformation functions. In creation of the restoration filters, several LPFs were tried. The choice of the restoration filters was based on improvement of contrast in the single-isotope ^{99m}Tc , 140-keV images and ^{18}F , 511-keV images. The restoration filters were created using the Butterworth LPF of order $n = 6$ and cutoff frequency of $f = 0.156$ cycles/pixel and the Butterworth LPF of order $n = 7$ and cutoff frequency of $f = 0.172$ cycles/pixel, which multiplied $1/\text{MTF}_{b2}$ and $1/\text{MTF}_{a1}$, respectively. For example, the theoretical Equation 19, in practice, was modified to:

$$F_b = G_{b2}/(\text{MTF}_{b2} * \text{LPF} + \gamma), \quad \text{Eq. 19a}$$

where LPF denotes the LPF used, and γ is as described above.

Figure 4A shows three 4×4 pixel regions of interest (ROIs), one over the left ventricle cavity (LVC), the second over the septum and the third over the lateral area of the myocardium. The average value from the last two ROIs was denoted as A, and the average value from the first ROI was B. The contrast between the LVC and the myocardium, defined as $C = (A - B)/(A + B)$, was used as a parameter to evaluate the results of the dual-isotope correction method with restoration. In Figure 5, the profiles

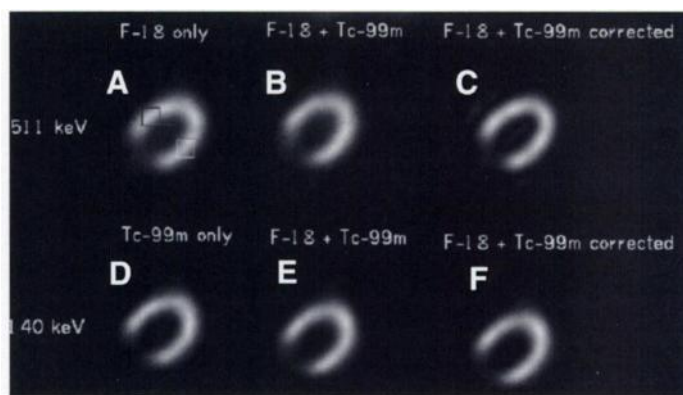


FIGURE 4. Transaxial slices through the heart phantom. (A) ^{18}F 511-keV image. (B) $^{18}\text{F} + ^{99m}\text{Tc}$ 511-keV image. (C) $^{18}\text{F} + ^{99m}\text{Tc}$ 511-keV corrected image. (D) ^{99m}Tc 140-keV image. (E) $^{18}\text{F} + ^{99m}\text{Tc}$ 140-keV image. (F) $^{18}\text{F} + ^{99m}\text{Tc}$ 140-keV corrected image.

through the same three ROIs shown in Figure 4A are given for 511-keV and 140-keV images.

RESULTS

The SPECT spatial resolution results for both ^{99m}Tc and ^{18}F point sources show that reconstructed PSF is much less spatial-variant than is the projection PSF. In Table 1, the resolution for

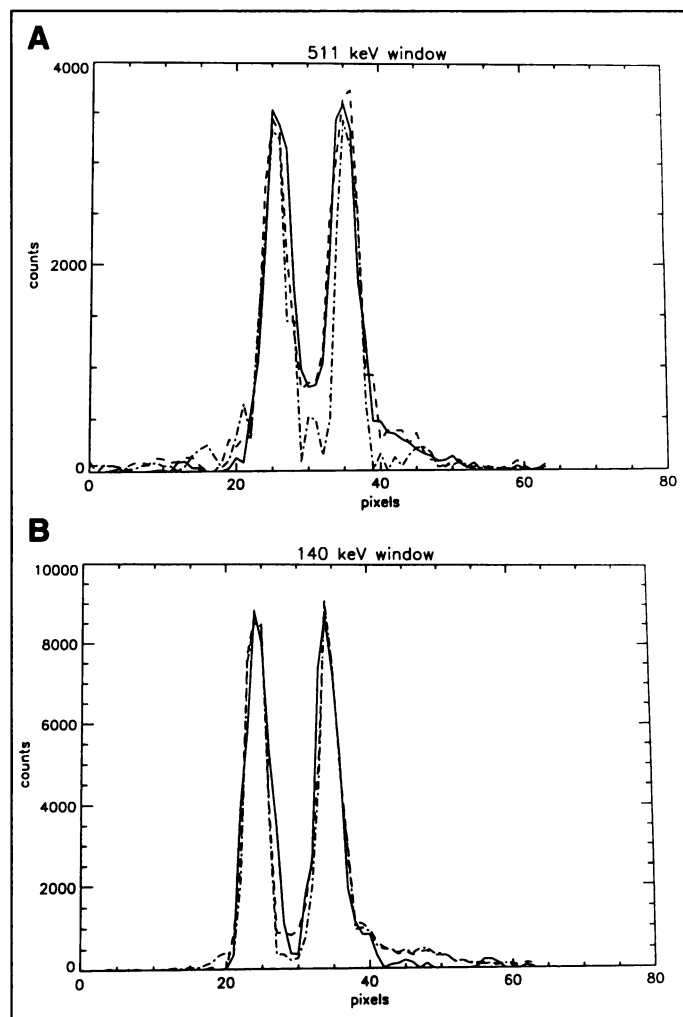


FIGURE 5. Profiles through the three ROIs shown in Figure 4A. (A) Profile through the ^{18}F 511-keV image (solid line), $^{18}\text{F} + ^{99m}\text{Tc}$ 511-keV image (dotted line) and $^{18}\text{F} + ^{99m}\text{Tc}$ 511-keV corrected image (dashed line). (B) ^{99m}Tc 140-keV image (solid line), $^{18}\text{F} + ^{99m}\text{Tc}$ 140-keV image (dotted line) and $^{18}\text{F} + ^{99m}\text{Tc}$ 140-keV corrected image (dashed line).

TABLE 1

SPECT Spatial Resolution Measured as FWHM (mm) for Fluorine-18 Point Sources at the 511-keV Energy Window

Distance (cm)	FWHM (mm), radial component	FWHM (mm), tangential component
0.0	23.3	23.3
2.5	23.4	23.1
5.0	23.5	22.9
7.5	24.1	20.3
9.0	24.5	18.8

The s.d. was less than 0.7 mm in all measurements and was obtained from three measurements.

the ^{18}F reconstructed point source at the 511-keV window is given. The same results for the $^{99\text{m}}\text{Tc}$ point source at 140-keV window are given in Table 2.

The cross-talk fractions were measured as a fraction of the total counts in the scatter compared to the primary window reconstructed transaxial images (Butterworth filter, fifth order, 0.23 cutoff frequency). The cross-talk fraction of ^{18}F was slightly higher in the 140-keV window (Fig. 6A; 0.47 ± 0.02) than it was in the 250-keV window (Fig. 6B; 0.35 ± 0.01), mostly due to the contribution of the back-scatter, which, for 511-keV photons, has a peak at 170 keV (Fig. 1). The cross-talk fraction of $^{99\text{m}}\text{Tc}$ into the 511-keV window was negligible (0.002 ± 0.0001) for the same reconstruction Butterworth filter.

Because the $^{99\text{m}}\text{Tc}$ cross-talk into the 511-keV window was negligible, the contrast between the LVC and the myocardium was almost the same with the 511-keV ^{18}F image (Fig. 4A; 0.59) and the dual-isotope ($^{18}\text{F} + ^{99\text{m}}\text{Tc}$), 511-keV image (Fig. 4B; 0.60) (Table 3 and Fig. 5A). Practically the same contrast, 0.61, was measured in the cross-talk corrected dual-isotope ($^{18}\text{F} + ^{99\text{m}}\text{Tc}$), 511-keV image (Table 3). The improvement of the contrast in the corrected dual-isotope ($^{18}\text{F} + ^{99\text{m}}\text{Tc}$), 511-keV

TABLE 2

SPECT Spatial Resolution Measured as FWHM (mm) for Technetium-99m Point Sources at the 140-keV Energy Window

Distance (cm)	FWHM (mm), radial component	FWHM (mm), tangential component
0.0	15.1	15.1
2.5	15.8	15.0
5.0	17.1	14.4
7.5	17.6	12.5
9.0	18.2	11.4

The s.d. was less than 0.7 mm in all measurements and was obtained from three measurements.

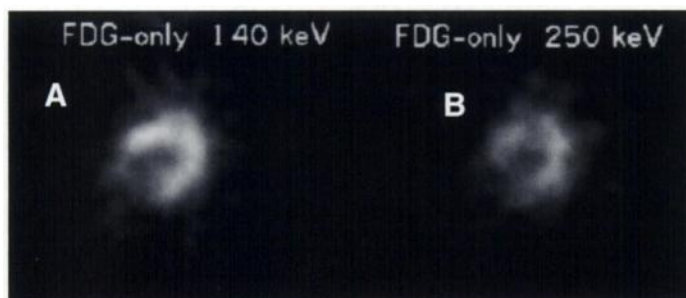


FIGURE 6. Transaxial slices through the heart phantom. A cross-talk of the ^{18}F in the 140-keV window (A) and 250-keV window (B).

TABLE 3

Contrast Between Left Ventricle Cavity and Myocardium in the 511-keV Images

Imaging	Contrast
^{18}F single-radionuclide	0.59 ± 0.01
Dual-radionuclide ($^{18}\text{F} + ^{99\text{m}}\text{Tc}$)	0.60 ± 0.03
$^{18}\text{F} + ^{99\text{m}}\text{Tc}$, cross-talk-corrected only	0.61 ± 0.05
$^{18}\text{F} + ^{99\text{m}}\text{Tc}$, cross-talk + restoration correction	0.74 ± 0.05
^{18}F and restoration-corrected only	0.74 ± 0.02

image (Fig. 4C and Fig. 5A) to the value of 0.74 (Table 3) is exclusively a result of the restoration correction. The restoration corrected single-isotope ^{18}F image had the same contrast, 0.74 (Table 3).

In the transaxial dual-isotope ($^{18}\text{F} + ^{99\text{m}}\text{Tc}$), 140-keV image, the ^{18}F cross-talk into the 140-keV window (Fig. 6A) decreased the contrast between LVC and myocardium. This resulted in a contrast value of 0.78 as compared with 0.87, which was the contrast in the 140-keV, single-isotope $^{99\text{m}}\text{Tc}$ image (Table 4 and Fig. 5B). However, in the corrected dual-isotope ($^{18}\text{F} + ^{99\text{m}}\text{Tc}$), 140-keV image (Fig. 4F), the contrast was improved to 0.92 (Table 2 and Fig. 5B), which was slightly better than that in the uncorrected 140-keV, single-isotope $^{99\text{m}}\text{Tc}$ image (0.87; Table 4). Here, both the restoration and cross-talk correction contributed. Without the restoration, i.e., with only cross-talk correction, the improvement of the contrast in the corrected dual-isotope ($^{18}\text{F} + ^{99\text{m}}\text{Tc}$), 140-keV image was 0.85 (Table 4). This is slightly lower than the contrast value in the uncorrected 140-keV, single-isotope $^{99\text{m}}\text{Tc}$ image. The contrast in the 140-keV, single-isotope $^{99\text{m}}\text{Tc}$ image after restoration correction improved to 0.95 from 0.87 and was slightly higher than in the corrected dual-isotope ($^{18}\text{F} + ^{99\text{m}}\text{Tc}$), 140-keV image (0.92; Table 4).

Figure 7A shows dual-isotope ($^{18}\text{F} + ^{99\text{m}}\text{Tc}$), 250-keV image previously denoted as g_3 ; Figure 7B shows a transformation $W_1\{g_3\}$ of the image g_3 ; and Figure 7C shows a transformation $(I - W_1 \otimes U_2)^{-1}\{W_1\{g_3\}\}$ of the image g_3 . In the second row of Figure 7, there are absolute value differences, on pixel-by-pixel basis, of images normalized to the same ^{18}F activity. Figure 7D shows differences between ^{18}F cross-talk in 140-keV window (Fig. 6A) and transformed dual-isotope, 250-keV image, i.e., $(I - W_1 \otimes U_2)^{-1}\{W_1\{g_3\}\}$ (Fig. 7C). Figure 7E shows the same difference, but it is between ^{18}F cross-talk in the 250-keV window (Fig. 6B) and the $(I - W_1 \otimes U_2)^{-1}\{W_1\{g_3\}\}$ image (Fig. 7C). The last image in Figure 7, i.e., Figure 7F, shows differences between ^{18}F cross-talk in 140-keV window (Fig. 6A) and a scaled, by a factor of 1.34, dual-isotope, 250-keV image, g_3 (Fig. 7C). The factor 1.34 is the ratio of ^{18}F cross-talk factors in the 140-keV and 250-keV windows.

In addition, the image distance between ^{18}F 140-keV and 250-keV images and the dual-isotope, 250-keV image was calculated giving the results of 1715.0 and 5158.0, respectively.

TABLE 4

Contrast Between Left Ventricle Cavity and Myocardium in the 140-keV Image

Imaging	Contrast
$^{99\text{m}}\text{Tc}$ single-radionuclide	0.87 ± 0.01
Dual-radionuclide ($^{18}\text{F} + ^{99\text{m}}\text{Tc}$)	0.78 ± 0.02
$^{18}\text{F} + ^{99\text{m}}\text{Tc}$, cross-talk-corrected only	0.85 ± 0.04
$^{18}\text{F} + ^{99\text{m}}\text{Tc}$, cross-talk + restoration correction	0.92 ± 0.05
$^{99\text{m}}\text{Tc}$ and restoration-corrected only	0.95 ± 0.03

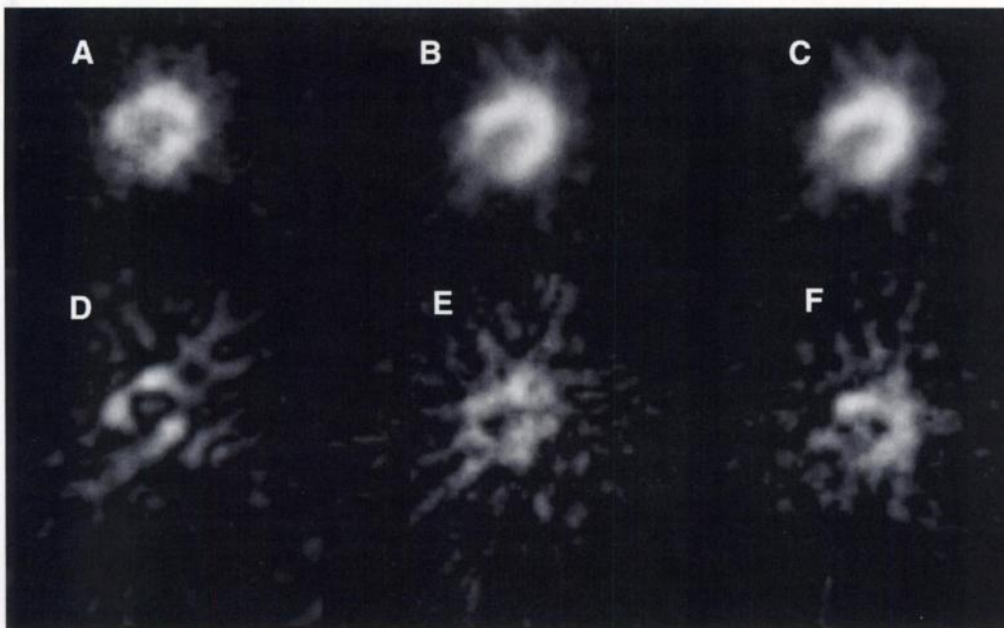


FIGURE 7. Transaxial slices through the heart phantom. (A) $^{18}\text{F} + ^{99\text{m}}\text{Tc}$ 250-keV image, i.e., g_3 . (B) The same image transformed with W_1 transformation, i.e., $W_1\{g_3\}$. (C) Image in A transformed with $(I - W_1 \otimes U_2)^{-1} \otimes W_1$ transformation, i.e., $(I - W_1 \otimes U_2)^{-1} \{W_1\{g_3\}\}$. (D) Difference between ^{18}F 140-keV cross-talk image and image in C. (E) Difference between the ^{18}F 250-keV cross-talk image and image in C. (F) Difference between the ^{18}F 140-keV cross-talk image and the scaled $^{18}\text{F} + ^{99\text{m}}\text{Tc}$ 250-keV image.

The same distance between the ^{18}F 140-keV image and the scaled dual-isotope, 250-keV image was 2868.2. The image distance is defined as, $\{\sum_{ij} (x_{ij} - y_{ij})^2\}^{-1/2}$, where x_{ij} and y_{ij} are values at the (ij) pixel of the images $X = (x_{ij})$ and $Y = (y_{ij})$, respectively.

DISCUSSION

In the simultaneous, dual-isotope imaging, in which the primary energy windows of the isotopes used are distant (e.g., $^{201}\text{Tl}/^{99\text{m}}\text{Tc}$, $^{201}\text{Tl}/^{111}\text{In}$ and $^{18}\text{F}/^{99\text{m}}\text{Tc}$), it is possible to use the third energy window, placed between the primary windows, to obtain additional information on the cross-talk. Figure 6 shows the cross-talk of the ^{18}F into the 140-keV and 250-keV windows. The cross-talk in the 140-keV window slightly higher and spatially different than the 250-keV cross-talk. The idea behind the three-window cross-talk correction was to use the third-window image to estimate the cross-talk in the other isotope's primary window. However, instead of simple scaling, here, we are taking into account the difference in the spatial distribution between the 250-keV and 140-keV ^{18}F cross-talk.

The difference between simple scaling and the transformation approach is shown in Figure 7. Both approaches use dual-isotope, 250-keV image, g_3 , to estimate ^{18}F 140-keV cross-talk (Fig. 6A). Figure 7B and Figure 7C show the effect of the W_1 and $(I - W_1 \otimes U_2)^{-1} \otimes W_1$ transformations on the image g_3 , respectively. Although the same transformation $(I - W_1 \otimes U_2)^{-1}$ has to be applied to the g_2 (Eq. 13), the image $(I - W_1 \otimes U_2)^{-1} \{W_1\{g_3\}\}$, shown in Figure 7C, approximates ^{18}F 140-keV cross-talk. This approximation image has been compared with measured ^{18}F 140-keV and 250-keV cross-talk images (Fig. 6, A and B, respectively), showing that it is closer to the 140-keV than it is to the 250-keV ^{18}F image (Fig. 7, D and E). The calculated corresponding distances, 1715.0 and 5158.0, confirmed this conclusion. The scaled dual-isotope, 250 keV image, g_3 , subtracted from the measured ^{18}F 140 keV cross-talk image (Fig. 7F) showed a greater difference than when the image $(I - W_1 \otimes U_2)^{-1} \{W_1\{g_3\}\}$ was subtracted from the same ^{18}F 140-keV cross-talk image, and the calculated difference, 2868.2, was significantly higher than the same difference with the transformation approach (1715.0). The results presented in Figure 7, as well as calculated differences, shows that scaling approach is inferior to the transformation approach, which, in addition to proper scaling, takes into

account differences in spatial distribution. The main disadvantage of the scaling approach is that it neglects differences in spatial distribution of the cross-talk in different energy windows.

The choice of the collimator in the dual-isotope imaging becomes a problem when the primary energy windows of the isotopes used are very distant (e.g., $^{201}\text{Tl}/^{111}\text{In}$ and $^{18}\text{F}/^{99\text{m}}\text{Tc}$). Usually, the collimator is designed to suppress septal penetration of the higher-energy isotope. However, in 511-keV imaging, the septal penetration is still high due to the inadequacy of present day scintillation cameras for such imaging and to the limitations in the collimator design (e.g., weight). Moreover, the UHE collimator is not designed for the lower-energy isotope ($^{99\text{m}}\text{Tc}$ in our case). The restoration component of the described correction technique should significantly compensate for such a collimator in both primary energy windows. In the 511-keV window, the correction achieved was exclusively the result of the restoration (Fig. 4C) due to the fact that $^{99\text{m}}\text{Tc}$ cross-talk was negligible. In the 140-keV window, both the restoration and the cross-talk corrections contributed equally (Fig. 4F).

This correction method can be applied pre- or postreconstruction. However, we have used the postreconstruction correction method. There are two main reasons for such a choice. First, our results, in addition to previously published results, confirmed that the reconstructed PSF is less spatially variant than is the projection PSF (25). It seems that postreconstruction correction can provide reasonably good results in spite of the assumption of a spatially invariant system. Second, the hypothesis of the spatially invariant PSF can be challenged by determining spatially variant PSFs in all energy windows (26,27). Consequently, the spatially variant transfer functions and spatially variant restoration filters (28,29) can be obtained. The same approach can be generalized from the pixel, two-dimensional slice level to the voxel, three-dimensional entire object environment similar to the implementation of the three-dimensional nonuniform SPECT iterative reconstruction (30).

The description of the new correction method started with general transformations T_1 , T_2 , U_1 , U_2 , V_1 and V_2 . The solution for such a general approach was given with Equations 12 and 13. However, Equations 12 and 13 are complex, and to reduce them to Equations 16 and 17, we had to assume that the transformations T_1 , T_2 , U_1 , U_2 , V_1 and V_2 were linear and

spatially invariant. The assumption that the detection system, which is characterized by its PSF, is spatially invariant is the main limitation of this approach (1). However, the corrected images obtained by the described method have not shown any obvious artifacts. They were neither distorted nor more noisy compared with single-isotope images. Distortion was assessed visually in our phantom study and the root-mean-square (rms) noise, expressed as $\text{rms}\% = \{\sum_{ij} (x_{ij} - \text{avg}(x))^2\}^{1/2} / \text{avg}(x) \cdot 100\%$, was used in the uniform ROI of the myocardium as a parameter to investigate the amount of noise.

CONCLUSION

The results of our cardiac phantom dual-isotope $^{18}\text{F}/^{99\text{m}}\text{Tc}$ study show that the new three-window transformation cross-talk correction method with restoration can significantly improve simultaneous, dual-isotope images. The corrected dual-isotope images, due to the restoration component in the new correction technique, can have even better contrast than do the corresponding uncorrected single-isotope images.

ACKNOWLEDGMENTS

We thank Michael Muzinic, CNMT, RT(N); Peter Webner, CNMT, RT(N); and Ian Zolty, CNMT, RT(N), for the help in the phantom and point-source acquisitions.

APPENDIX

Derivation of the Three-Window Transformation Cross-Talk Correction Equations

Equations 1 and 3 can, by using Equations 7 and 8, be rewritten to:

$$g_1 = g_{a1} + W_2\{g_{b3}\}, \quad \text{Eq. 1a}$$

$$g_3 = U_1\{g_{a1}\} + g_{b3}. \quad \text{Eq. 2a}$$

Now, transformation W_2 can be applied on both sides of Equation 2a, and Equation 2a can be subtracted from Equation 1a, giving:

$$g_1 - W_2\{g_3\} = \{I - W_2 \odot U_1\} \{g_{a1}\} \quad \text{Eq. 12a}$$

which, by simply switching the sides and applying $\{I - W_2 \odot U_1\}^{-1}$ on both sides, becomes Equation 12. In the same way, Equation 13 can be obtained using Equations 1, 2, 6 and 9.

REFERENCES

1. Knešarek K. A new dual-isotope convolution cross-talk correction method: a Tl-201/Tc-99m cardiac phantom study. *Med Phys* 1994;21:1577-1583.
2. Ivanovic M, Weber DA, Loncaric S, Franceschi D. Feasibility of dual radionuclide brain imaging with I-123 and Tc-99m. *Med Phys* 1994;21:667-674.
3. Devous M, Payne J, Lowe J. Dual-isotope brain SPECT imaging with technetium-99m and iodine-123: clinical validation using xenon-133 SPECT. *J Nucl Med* 1992;33:1919-1924.
4. Sandrock D, Merino MJ, Norton JA, Neumann RD. Parathyroid imaging by Tc/Tl scintigraphy. *Eur J Nucl Med* 1990;16:607-613.
5. Klumper A, Zwijnenburg A. Dual isotope ($^{81\text{m}}\text{Kr}$ and $^{99\text{m}}\text{Tc}$) SPECT in lung function diagnosis. *Phys Med Biol* 1986;7:751-761.

6. Johnson LL, Seldin DW. The role of antimyosin antibodies in acute myocardial infarction. *Semin Nucl Med* 1989;19:238-246.
7. Johnson LL, Seldin DW, Keller AM, et al. Dual-isotope thallium and indium antimyosin SPECT imaging to identify acute infarct patients at further ischemic risk. *Circulation* 1990;81:37-45.
8. Schroeder H, Top H, Frederick M, et al. Thallium and indium antimyosin dual-isotope single-photon emission tomography in acute myocardial infarction to identify patients at further ischemic risk. *Eur J Nucl Med* 1994;21:415-422.
9. Kitahara K, Suzuki S, Takayama Y, et al. New color imaging of [$^{99\text{m}}\text{Tc}$]pyrophosphate and [^{201}Tl]chloride dual-isotope single photon emission computed tomography in acute myocarditis. *Jap J Nucl Med* 1989;26:773-779.
10. Kawaguchi K, Sone T, Tsuboi H, et al. Quantitative estimation of infarct size by simultaneous dual radionuclide single photon emission computed tomography: comparison with peak serum creatine kinase activity. *Am Heart J* 1991;121:1353-1360.
11. Kiat H, Germano G, Friedman J, et al. Comparative feasibility of separate or simultaneous rest thallium/stress technetium-99m-sestamibi dual-isotope myocardial perfusion SPECT. *J Nucl Med* 1994;35:542-548.
12. Heo J, Wolmer I, Kegel J, Iskandrian AS. Sequential dual-isotope SPECT imaging with thallium-201 and technetium-99m-sestamibi. *J Nucl Med* 1994;35:549-553.
13. Stoll H-P, Hellwing N, Alexander C, Ozbek C, Schieffer H, Oberhausen E. Myocardial metabolic imaging by means of fluorine-18-deoxyglucose/technetium-99m sestamibi dual-isotope single-photon emission tomography. *Eur J Nucl Med* 1994;21:1085-1093.
14. Burt RW, Perkins OW, Oppenheim BE, et al. Direct comparison of F-18-FDG SPECT, F-18-FDG PET and rest-thallium SPECT for detection of myocardial viability. *J Nucl Med* 1995;36:176-179.
15. Delbecke D, Videlefsky S, Patton JA, et al. Rest myocardial perfusion/metabolism imaging using simultaneous dual-isotope acquisition SPECT with technetium-99m-MIBI/fluorine-18-FDG. *J Nucl Med* 1995;36:2110-2119.
16. Yang DC, Ragasa E, Gould L, et al. Radionuclide simultaneous dual-isotope stress myocardial perfusion study using "three-window technique." *Clin Nucl Med* 1993;18:852-857.
17. Hademenos GJ, Dahlbom M, Hoffman EJ. Simultaneous dual-isotope technetium-99m/thallium-201 cardiac SPECT imaging using a projection-dependent spill-down correction factor. *Eur J Nucl Med* 1995;5:465-472.
18. Moore SC, English RJ, Syraevan C, et al. Simultaneous Tc-99m/Tl-201 imaging using energy-based estimation of the spatial distributions of contaminant photons. *IEEE Trans Nucl Sci* 1995;44:1189-1195.
19. King AM, Schwinger RB, Doherty PW, Penney BC. Two dimensional filtering of SPECT images using the Metz and Wiener filters. *J Nucl Med* 1984;25:1234-1240.
20. Webb S, Long AP, Ott RJ, Leach MO, Flower MA. Constrained deconvolution of SPECT liver tomograms by direct digital image restoration. *Med Phys* 1985;12:53-58.
21. King AM, Schwinger RB, Penney BC, Doherty PW, Bianco JA. Digital restoration of indium-111 and iodine-123 images with optimized Metz filters. *J Nucl Med* 1986;27:1327-1336.
22. Yanch JC, Irvine AT, Webb S, Flower MA. A comparison of deconvolution and windowed subtraction techniques for scatter compensation in SPECT. *IEEE Trans Med Imag* 1988;7:13-20.
23. Penney BC, King MA, Schwinger RB, Baker SP, Doherty PW. Modifying constrained least-square restoration for application to SPECT projection images. *Med Phys* 1988;15:334-342.
24. Tihonov AN, Arsenin VY. *Solutions of ill-posed problems*. Washington DC: Winston; 1977:25-32.
25. Glick SJ, King MA, Knešarek K, Burbank K. An investigation of the stationary of the 3D modulation transfer function of SPECT. *IEEE Trans Nucl Sci* 1989;36:973-977.
26. Knešarek K, King MA, Glick SJ, Penney CB. A 3-D non-stationary simulation of SPECT imaging. *J Nucl Med* 1989;30:881.
27. Knešarek K. Two new experimental methods of calculating scatter fraction as a function of depth in scattering media: a comparison study. *Med Phys* 1992;19:591-598.
28. Todd-Pokropek A. Non-stationary deconvolution using a multi-resolution stack. In: de Graf CN, Viergever MA, eds. *Proceedings of the 10th international conference on information processing in medical imaging*. New York: Plenum Press; 1988:277-290.
29. Bouffelfel D, Rangayyan RM, Hahn LJ, Kloiber R, Kuduvali GR. Two-dimensional restoration of SPECT images using the Kalman filter. *IEEE Trans Med Imag* 1994;13:102-109.
30. Gilland DR, Jaszczak RJ, Wang H, Turkington TG, Greer KL, Coleman RE. A 3D model of non-uniform attenuation and detector response for efficient iterative reconstruction in SPECT. *Phys Med Biol* 1994;39:547-561.